



## Silicate weathering machine at work: Rock magnetic data from the late Paleocene–early Eocene Cicogna section, Italy

**Edoardo Dallanave**

*Department of Geosciences, University of Padova, Via Giotto 1, I-35137 Padua, Italy*

*Alpine Laboratory of Paleomagnetism, Via Madonna dei Boschi 76, I-12016 Peveragno, Italy  
(edoardo.dallanave@unipd.it)*

**Lisa Tauxe**

*Scripps Institution of Oceanography, UCSD, 9500 Gilman Drive, La Jolla, California 92093-0220, USA*

**Giovanni Muttoni**

*Alpine Laboratory of Paleomagnetism, Via Madonna dei Boschi 76, I-12016 Peveragno, Italy*

*Department of Earth Sciences, University of Milan, Via Mangiagalli, 34 I-20133 Milan, Italy*

**Domenico Rio**

*Department of Geosciences, University of Padova, Via Giotto 1, I-35137 Padua, Italy*

[1] We describe a scenario of climate forcing on sedimentation recorded in the late Paleocene–early Eocene Cicogna marine section from the Belluno Basin (NE Italy). Previously published magneto-biostratigraphic data revealed that the ~81 m Cicogna section extends from Chron C25r to Chron C23r spanning the NP7/NP8–NP12 nanofossil zones (~52.2–56.6 Ma). Using previously published rock magnetic data, augmented by data from this study, we describe and thoroughly discuss a pronounced increase of hematite (relative to maghemite or magnetite) between ~54.9 and 54.6 Ma immediately above the Paleocene–Eocene boundary, followed by a second, long-term increasing trend from ~54 Ma up to ~52.2 Ma in the early Eocene. This hematite is essentially of detrital origin, insofar as it is associated with a strong shallow bias of paleomagnetic inclinations, and is interpreted to have formed on land by the weathering of Fe-bearing silicates and other primary minerals. We speculate that the warm and humid climate typical of the Paleocene–Eocene thermal maximum (PETM, ~54.9 Ma) as well as of the warming trend leading to the early Eocene climatic optimum (EECO; ~52–50 Ma) enhanced continental weathering of silicate rocks with the consequent production, transport, and sedimentation of detrital hematite grains. This hypothesis is confirmed by a statistical correlation between the rock magnetic properties and global climate as revealed by a standard benthic oxygen isotope record from the literature. Our temporal coupling between oxidation state of sedimentary magnetic phases and global climate is therefore consistent with the existence in the Paleocene–Eocene of the silicate weathering negative feedback mechanism for the long-term stabilization of the Earth's surface temperature.

**Components:** 7800 words, 8 figures, 1 table.

**Keywords:** Paleocene; Eocene; global warming; silicate weathering; hematite; maghemite.

**Index Terms:** 1512 Geomagnetism and Paleomagnetism: Environmental magnetism (1635); 1540 Geomagnetism and Paleomagnetism: Rock and mineral magnetism (1635); 1616 Global Change: Climate variability (1635).

**Received** 22 March 2010; **Revised** 1 June 2010; **Accepted** 9 June 2010; **Published** 17 July 2010.

Dallanave, E., L. Tauxe, G. Muttoni, and D. Rio (2010), Silicate weathering machine at work: Rock magnetic data from the late Paleocene–early Eocene Cicogna section, Italy, *Geochem. Geophys. Geosyst.*, *11*, Q07008, doi:10.1029/2010GC003142.

## 1. Introduction

[2] During the Cenozoic, Earth's climate underwent a significant long-term evolution, evolving from non-glacial states, with virtually no ice at sea level, to polar-glacial conditions [e.g., Zachos et al., 2001; Miller et al., 2005]. The late Paleocene–early Eocene was characterized by a global warming trend that eventually culminated with the early Eocene climatic optimum (EECO, ~52–50 Ma). The EECO was characterized by warm climatic conditions even at extremely high latitudes [McKenna, 1980; Moran et al., 2006]. Atlantic bottom waters reached temperatures of 14°C, as indicated by oxygen stable isotope data [Zachos et al., 2001; Miller et al., 2005], and promoted the widespread deposition of silica [Muttoni and Kent, 2007]. The long-term late Paleocene–early Eocene warming trend was punctuated by several short-lived hyperthermal events [Cramer et al., 2003]. The most prominent of these episodes was the Paleocene–Eocene thermal maximum (PETM) [e.g., Kennett and Stott, 1991]. The PETM is marked by a 2‰–4‰ global negative carbon isotope excursion (CIE) [Kennett and Stott, 1991; Koch et al., 1992; Zachos et al., 2003] and extensive carbonate dissolution of deep-sea sediments [Zachos et al., 2005]. The CIE was interpreted as an event of massive injection of light carbon into the ocean/atmosphere reservoir, the origin and triggering mechanisms of which are still a matter of debate [e.g., Dickens et al., 1995; Kent et al., 2003; Svensen et al., 2004; Cramer and Kent, 2005; Pagani et al., 2006]. Existing records reveal that during the PETM, deep-sea temperatures increased by 5–6°C in less than 10 kyr [Kennett and Stott, 1991; Bralower et al., 1995; Thomas and Shackleton, 1996], whereas sea-surface temperatures increased by 8°C at high latitudes [Kelly et al., 1996; Dingle et al., 1998; Thomas and Bralower, 1999; Pearson et al., 2001; Zachos et al., 2001]. Both marine and continental PETM records registered an increase in climate humidity [Bolle and Adate, 2001; Bowen et al., 2004], also at high latitudes [Robert and Kennett, 1994], and a marked increase in seasonal precipitation [Schmitz and

Pujalte, 2007]. The PETM recovery was gradual and the total duration of the stable isotope excursion is estimated to be on the order of ~200 kyr, although different authors proposed somewhat different timings [Giusberti et al., 2007; Röhl et al., 2007].

[3] EECO and PETM warm and humid climates were probably related to high greenhouse gas concentrations. This is supported by the occurrence of high (albeit highly scattered)  $p\text{CO}_2$  estimates on the order of >1000 ppm at around the EECO [e.g., Yapp, 2004; Lowenstein and Demicco, 2006]. The EECO long-term warmth ended at ~50 Ma in the early Eocene with the onset of a long-term cooling trend that continued over the ensuing middle to late Eocene and culminated with the inception of major Antarctic ice sheets at Oi-1 near the Eocene–Oligocene boundary at ~34 Ma [Miller et al., 1991; Zachos et al., 2001]. This long-term cooling trend was probably due to a progressive decrease of greenhouse gas in the atmosphere reservoir, as broadly indicated by generally low (<500 ppm)  $p\text{CO}_2$  levels after Oi-1 [Pagani et al., 2005]. The long-term cooling was possibly caused by a perturbation of the  $\text{CO}_2$  input-output balance triggered by the collision of India with Asia at ~50 Ma [Kent and Muttoni, 2008].

[4] EECO and PETM warm and humid climates should be characterized by enhanced land weathering rates, which would promote the sequestration of excess  $\text{CO}_2$  by chemical weathering of silicates followed by the deposition of carbonates, in accordance with the negative feedback mechanism for the long-term stabilization of the Earth's surfaces temperature originally proposed by Walker et al. [1981] [see also Kump et al., 2000]. Enhanced land weathering rates of Fe-bearing silicates should be accompanied by the production of Fe-oxides with high oxidation states as residuals of the weathering reactions. These Fe-oxides may be mobilized, transported, and deposited in adjacent sedimentary basins by the accelerated hydrological cycle and enhanced runoff typical of the EECO and PETM climates [Robert and Kennett, 1994; Sloan and

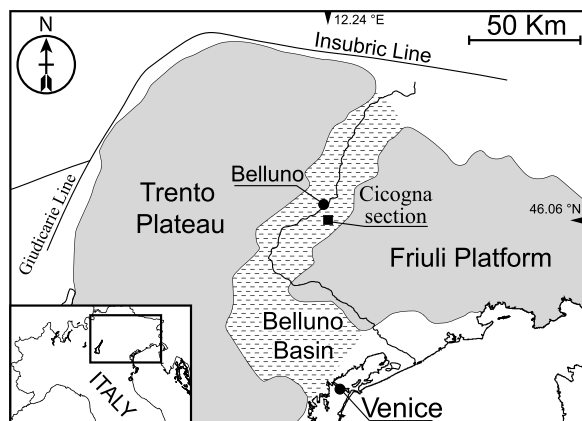


**Figure 1.** Main paleogeographic domains of the Venetian Southern Alps. The Cicogna section (Lat. = 46.06°N; Long. = 12.24°E) is located in the Belluno Basin, ~8 km to the south of the town of Belluno, along the Cicogna riverbed.

Rea, 1996; Bolle and Adatte, 2001; Bowen et al., 2004].

[5] In this paper, we use rock magnetic data from the marine Cicogna section (Belluno Basin, Northern Italy) of Dallanave et al. [2009], augmented by new data and statistical analyses from this study, to gauge the temporal relationship between rock magnetic properties and global climate as revealed by the oxygen isotopes record of Zachos et al. [2001] during the late Paleocene–early Eocene.

## 2. Geological Setting

[6] The Belluno Basin (Venetian Southern Alps, NE Italy), a paleogeographic domain developed since the Early Jurassic between the Trento Plateau and the Friuli Platform [Winterer and Bosellini, 1981; Castellarin and Cantelli, 2000] (Figure 1), is characterized by a 200–250 m-thick succession of Cretaceous–early Eocene hemipelagic sediments. These are mainly represented by well-bedded, pink to red limestones and marly limestones (Scaglia Rossa *sensu lato*, which comprises several local informal lithostratigraphic units [Di Napoli Alliata et al., 1970; Costa et al., 1996]).

[7] The Cicogna section consists of ~81 m of marly limestones referred to as the Scaglia Rossa (*s.l.*) Formation (locally named *Marna della Vena d'Oro*), overlain by the siliciclastic deposits of the Belluno Flysch. The section, extensively studied for magneto-biostratigraphy by Dallanave et al. [2009], extends in stratigraphic continuity from Chron C25r to Chron

C23r and from nannofossil zone NP7/NP8 to NP12 (=CP6–CP10), thus covering an interval of time between ~56.6 and ~52.2 Ma (Figure 2) according to the time scale of Berggren et al. [1995]. The basal ~15 m of the section are made of a rhythmic alternation of gray-greenish marly limestone-marl couplets; from ~15 to 20 m, the rhythmicity becomes progressively less apparent and the sediments gradually turn to pink-reddish marly limestones. The marly limestone sedimentation is abruptly interrupted at 28.7 m by a ~3 m-thick package of mainly red marly clays and marls hereafter referred to as the clay marl unit (CMU) (Figures 2a and 2b). The CMU starts with a ~2.5 cm-thick mottled red and gray-greenish clay level, overlain up to ~31.7 m by red marls flecked by rare gray-greenish patches, e.g., at ~29.05 m and ~30.8 m (Figure 2b). The Paleocene–Eocene boundary falls at the base of the CMU at Cicogna as well as elsewhere in the Belluno Basin [Arenillas et al., 1999; Agnini et al., 2006; Giusberti et al., 2007; Dallanave et al., 2009]. Giusberti et al. [2007] found a  $\delta^{13}\text{C}$  negative shift of 2.35‰ at the CMU base, and proposed that the CMU is related to the widespread acidification of the ocean waters [Zachos et al., 2005] and the associated dissolution of deep-sea carbonates that occurred during the PETM.

[8] From the top of the CMU at 31.7 m upward, the Cicogna section is made of pink-reddish marly limestone-marl couplets persisting up to 39.2 m. From 39.2 m up to ~75.0 m, the succession is dominated by red marls with no apparent rhythmicity, and is characterized by the presence of occasional gray-greenish levels and spots, often associated with bioturbation. From ~75 m to ~81 m, the section consists of red marls alternating with siliciclastic layers, which become dominant from 80.6 m (formal base of the Belluno Flysch) upwards.

## 3. Material and Methods

[9] To define the magnetic properties of the sediments, Dallanave et al. [2009] collected a total of 450 samples along the ~81 m of the Cicogna section. On these (weighted) samples, the low susceptibility and the isothermal remanence magnetization (IRM) imparted in 0.1 T and 1.0 T fields ( $\text{IRM}_{0.1\text{ T}}$  and  $\text{IRM}_{1.0\text{ T}}$ , respectively) were measured at the Alpine Laboratory of Paleomagnetism [Dallanave et al., 2009]. To better characterize the magnetic properties of the sediments, a new set of samples were studied at the paleomagnetic laboratory of

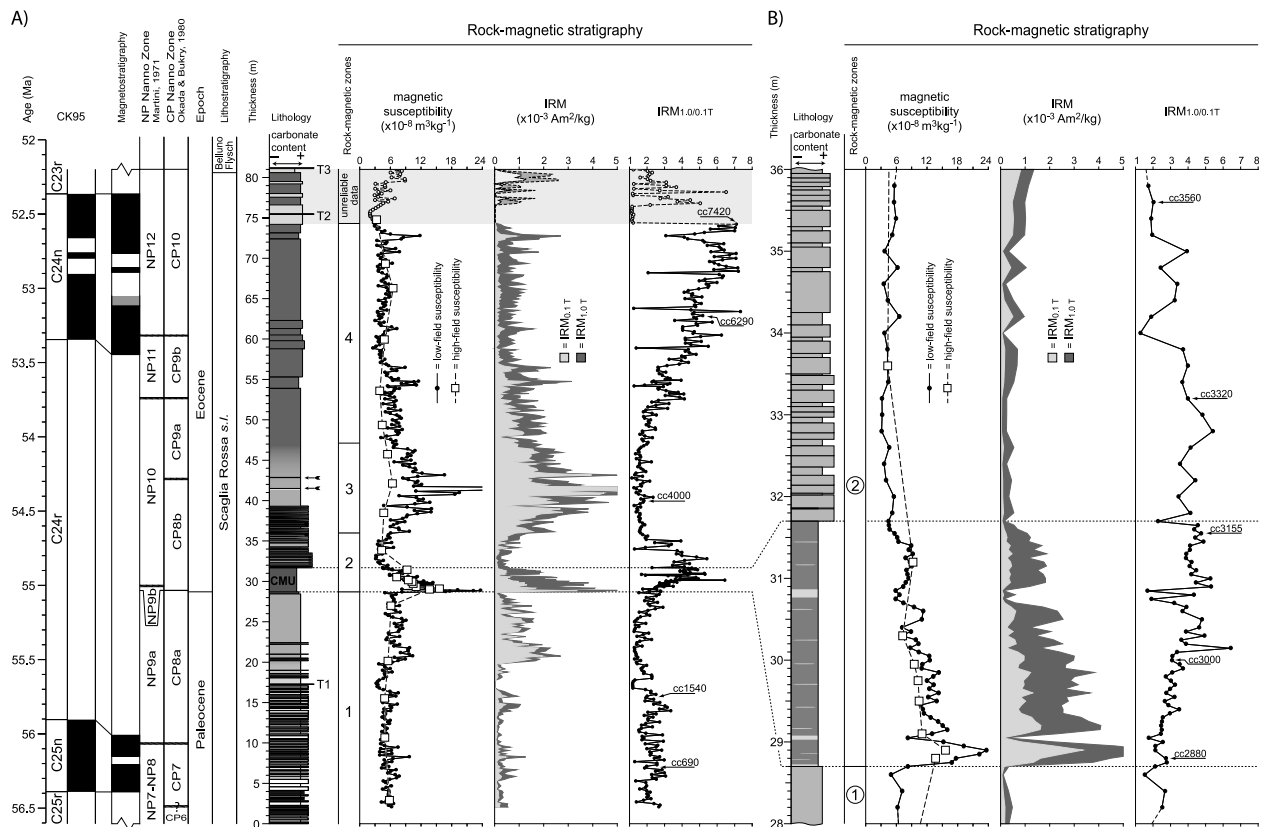


**Figure 2.** (a) The late Paleocene–early Eocene Cicogna section. Form left to right: chronological and magneto-biostratigraphical framework (for details, see *Dallanave et al.* [2009]); lithostratigraphic log of the section (T1 = Carbonate turbidite level; T2, T3 = Sandy turbidite levels; black arrows = calcite veins; CMU = clay marl unit); rock magnetic zonation across the section based on low- and high-field susceptibility, the IRMs at 0.1 T and 1.0 T fields, and their ratio ( $\text{IRM}_{1.0/0.1 \text{ T}}$ ). (b) Detail of the magnetic properties of the Cicogna section between 28 and 36 m (i.e., from the top of rock magnetic zone 1 to the top of the zone 2). See text for details.

the Scripps Institution of Oceanography (La Jolla, California). A total of 47 samples were magnetized in 2.5 T, 1.0 T, and 0.1 T along three orthogonal axes, and were successively subjected to alternating field (AF) demagnetization in 13 steps from 5 to 180 mT using a SI-4 specimen demagnetizer, with the resulting magnetization measured after each demagnetization step on a 2G DC-SQUID cryogenic magnetometer. After this procedure, the same samples plus 15 additional fresh samples ( $N = 62$ ) were magnetized in the same orthogonal fields (2.5 T, 1.0 T, and 0.1 T), and subjected to thermal demagnetization adopting 18 demagnetization steps from room temperature up to 670°C [Lowrie, 1990]. Hysteresis parameters were also obtained with a MICROMAG alternating gradient force magnetometer on a selected suite of 23 ~0.02–0.03 g specimens. Values of saturation magnetization ( $M_s$ ), saturation remanence ( $M_r$ ) and coercivity ( $B_c$ ) were

determined from the hysteresis loops after correction for a paramagnetic component observed in all samples. The values of the high-field magnetic susceptibility were estimated by calculating the slope of the linear (post-closure) portion of the hysteresis loops. The values of the coercivity of remanence ( $B_{cr}$ ) were estimated by calculating the parameter  $\Delta M$  obtained by subtracting the ascending (0–1 T) branch of the hysteresis loop from the descending (1–0 T) branch of the loop, with  $B_{cr}$  approximated by the field value at  $\Delta M = 50\%$  [Tauxe, 2010].

#### 4. Rock Magnetic Data

[10] The rock magnetic properties of the sediments are described hereafter by subdividing the Cicogna section from base to top into four rock magnetic zones (RMZ 1–4) (Figure 2 and Table 1).

**Table 1.** Rock Magnetic Values for Each Rock Magnetic Zone Described in the Text<sup>a</sup>

	Low-Field Susceptibility	High-Field Susceptibility	IRM <sub>0.1 T</sub>	IRM <sub>1.0 T</sub>	IRM <sub>1.0/0.1T</sub>
Zone 1 (0–28.7 m)					
Max	10.3	6.1	19.5	26.9	3.3
Min	3.2	4.9	0.2	0.2	1.2
Mean	5.9	5.5	3.4	5.9	2.0
St. Dev.	1.5	0.5	4.2	5.6	0.5
Zone 2 (28.7–36 m)					
Max	23.6	15.6	33.6	71.8	6.4
Min	3.1	4.3	0.4	0.8	0.9
Mean	9.1	10.2	6.1	17.7	3.4
St. Dev.	4.5	3.3	6.0	13.3	1.1
Zone 3 (36–47 m)					
Max	48.2	6.4	147	183	2.3
Min	4.7	4.7	2.3	2.9	1.1
Mean	11.2	5.5	20.6	31.5	1.6
St. Dev.	6.7	0.8	21.3	26.8	0.2
Zone 4 (47–74 m)					
Max	11.8	6.5	13.2	31.4	7.3
Min	2.6	3.3	0.4	0.5	1.2
Mean	5.6	4.7	3.4	10.5	4.1
St. Dev.	1.8	1.1	3.1	5.8	1.6

<sup>a</sup>Low- and high-field susceptibilities are expressed in  $10^{-8} \text{ m}^3 \text{ kg}^{-1}$ ; IRM<sub>0.1 T</sub> and IRM<sub>1.0 T</sub> are expressed in  $10^{-3} \text{ Am}^2 \text{ kg}^{-1}$ .

#### 4.1. Magnetic Susceptibility

[11] Within basal RMZ 1, the low-field and high-field magnetic susceptibilities are characterized by relatively low and similar values, reflecting the general control of paramagnetic minerals on the bulk susceptibility (Figure 2a and Table 1). The low-field susceptibility values show a marked negative swing in correspondence of the carbonate turbidite layer at ~17 m, and are slightly higher than average from ~20 m upwards, where the sediments turn from gray-greenish to pink-reddish in color. At the base of RMZ 2 (i.e., CMU base), the low-field susceptibility values abruptly rise, peaking at 28.9 m, i.e., ~0.2 m above the zone base. The high-field susceptibility rises as well, but it is consistently lower than the low-field susceptibility, indicating a main contribution from ferromagnetic (*s.l.*) minerals in the lower part of the CMU (Figures 2a and 2b). Above CMU peak values, the low- and high-field susceptibilities display a general decreasing trend, with two negative swings correlated with the gray-greenish levels observed at ~29 m and ~30.8 m. In correspondence of RMZ 3, the low-field susceptibility rises again, peaking at ~42 m, where carbonate dissolution surfaces were observed (Figure 2a); then, it gradually decreases, reaching relatively low and stable values from ~47 m (base of RMZ 4) up to the section top. The high-field susceptibility generally follows the same pattern, but in RMZ 3 it shows values constantly lower than the low-field susceptibility, which we interpret as due to the

presence of dominant ferromagnetic (*s.l.*) particles (Figure 2a).

#### 4.2. Coercivity and Unblocking Temperature Spectra

[12] Thermal and AF demagnetizations of three component-IRM reveal that the gray-greenish sediments from 0 to ~15 m within RMZ 1 are dominated by a 0.1 T magnetic coercivity phase (Figures 3a and 3b, sample cc690). This component gradually decreases in intensity during thermal demagnetization up to maximum unblocking temperatures of ~575°C, and is characterized by a virtually total drop of intensity after AF demagnetization fields of 100 mT; we interpret this fraction as magnetite. Subsidiary 1.0 T and a minor 2.5 T coercivity phases that persist up to 670°C are also present; the 1.0 T component drops by ~50% in AF fields of 180 mT, while the 2.5 T is not affected by the AF demagnetization procedure. These phases are interpreted as hematite. The dominance of the low coercivity magnetite phase in the first ~15 m of RMZ 1 is confirmed by the hysteresis loops, which, after paramagnetic correction, appear very narrow in shape (Figure 4, e.g., sample cc290). The measured Mr/Ms ratios are similar to those observed for a reference distribution data obtained from magnetite-bearing limestones [Channell and McCabe, 1994] (Figure 5).

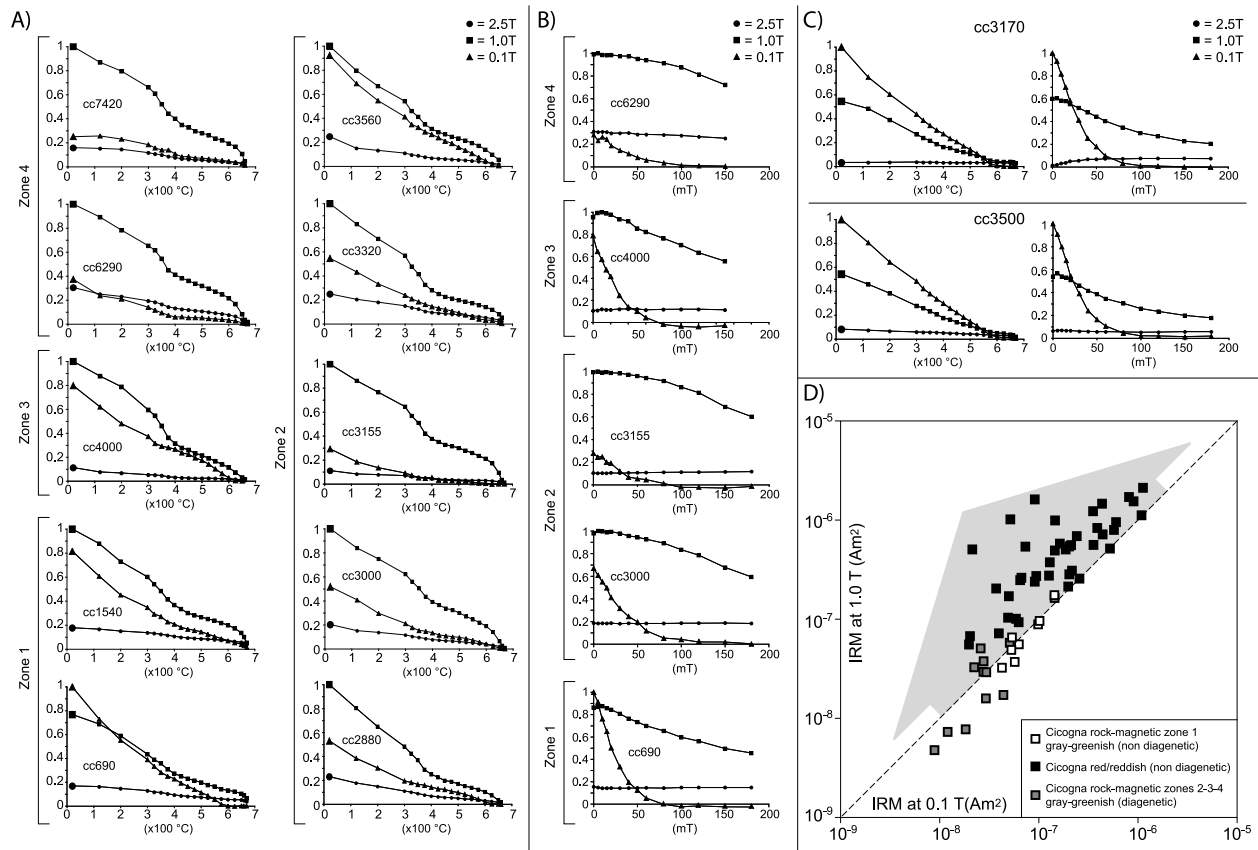


**Figure 3.** (a) Representative thermal demagnetization data of a three component IRM of samples from the Cicogna section. The stratigraphic position of the illustrated samples is indicated in Figures 2a and 2b. (b) Representative alternating field (AF) demagnetization data of three component IRM of samples from each rock magnetic zone of the Cicogna section; the correlative thermal demagnetization diagrams are shown in Figure 3a; the stratigraphic position is indicated in Figures 2a and 2b. (c) (left) Thermal and (right) AF demagnetization of three orthogonal IRMs of two representative samples collected from the gray-greenish spots in rock magnetic zone 2 at 31.7 m (cc3170) and 35.0 m (cc3500), respectively. (d) Logarithmic plot of IRMs at 1.0 T and 0.1 T of the thermally demagnetized samples; the gray-greenish samples collected from the diagenetic levels and spots of RMZ 2, 3 and 4 display generally the lowest values, whereas highest values are observed in red to reddish, non-diagenetic samples (the gray arrow marks the increase in the IRM at 1.0 T of the samples). See text for details.

[13] From ~15 m within RMZ 1 up to RMZ 4 at the section top, where the sediments are pink-reddish to red in color, thermal and AF demagnetizations of three component-IRM show that the 1.0 T coercivity fraction becomes dominant over a 0.1 T fraction of secondary importance. Thermal demagnetization data reveal that the dominant 1.0 T phase undergoes an intensity reduction between 300 and 400°C followed by a gentle but persistent further reduction up to 600°C and an abrupt final decrease to zero values up to ~670°C. During AF demagnetization, this coercivity phase drops by ~25% in fields of 180 mT. These behaviors are consistent with the presence of hematite. The smooth decrease observed in the 1.0 T curve between 300 and 400°C probably reflects a contribution from minor amounts of

maghemite that breaks down during heating in nearly zero magnetic field [e.g., Kodama, 1982; Wang et al., 2004]. This maghemite, picked up by the 1.0 T curve together with hematite, may speculatively reside within hematite grains (as residues of a maghemite → hematite phase transformation; see section 6). The 0.1 T fraction undergoes instead a smooth and persistent intensity decline during thermal demagnetization up to ~650–670°C. AF demagnetization reveals a virtually complete intensity loss at fields of 100 mT (Figures 3a and 3b, sample cc1540–7420). These behaviors are consistent with the presence of pure maghemite grains, which typically possesses low coercivity and Curie temperatures between 590 and 675°C [Tauxe, 2010]. Finally, a negligible 2.5 T fraction showing maximum unblocking temperatures

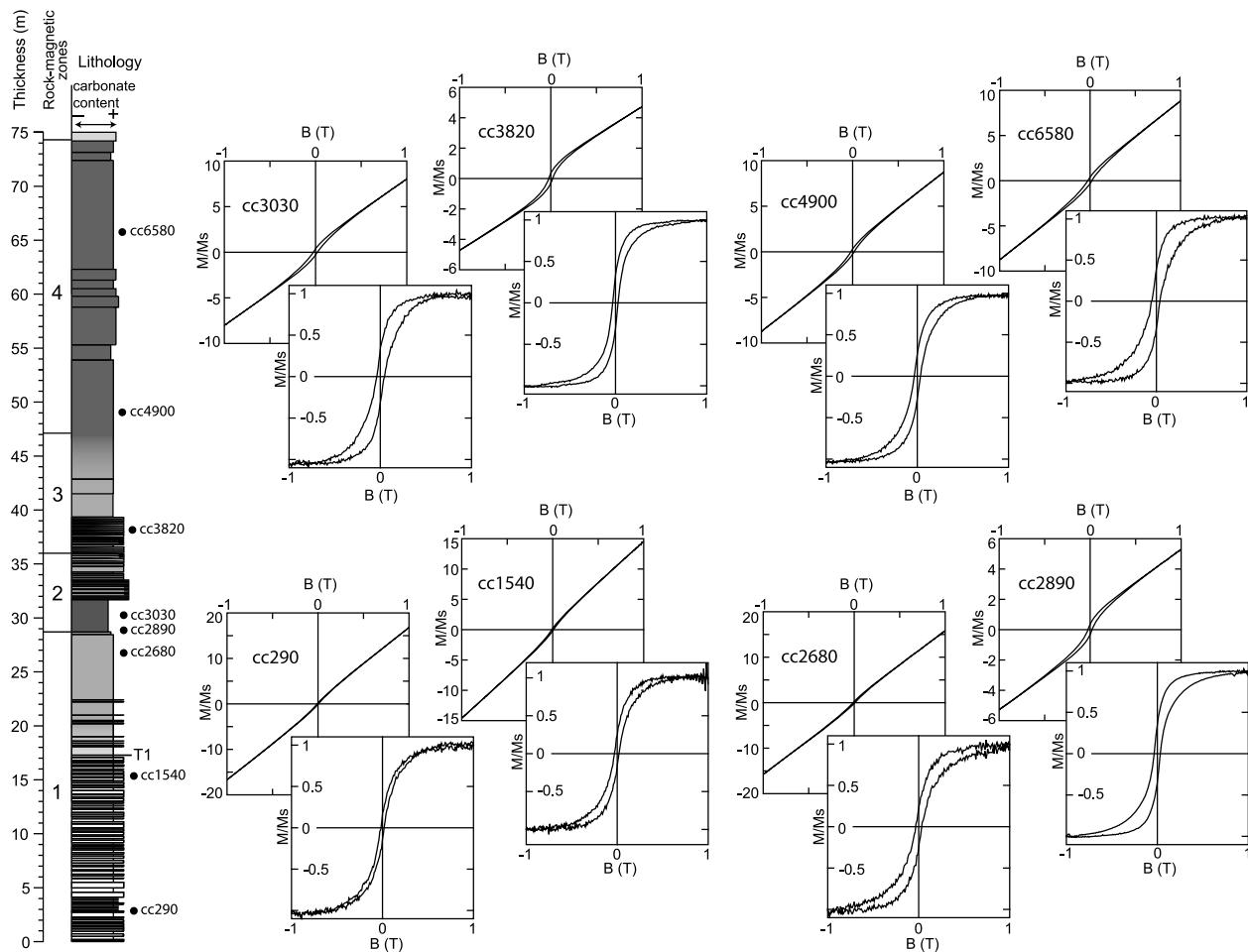


**Figure 4.** Hysteresis loops of representative samples from the Cicogna section with indication of stratigraphic position. The background and the foreground diagrams represent the loops before and after paramagnetic correction, respectively; the vertical axes of the diagrams represent the magnetization/saturation magnetization (M/Ms) ratio, while the horizontal axes the applied field (B) expressed in Tesla (T).

of  $\sim 670^\circ\text{C}$  and resistance to AF cleaning is also present and interpreted as hematite.

[14] The presence in these pink-reddish to red samples of distinct magnetic coercivity phases is confirmed by the hysteresis loops, which display typical wasp-waisted shapes [e.g., *Channell and McCabe, 1994; Muttoni, 1995; Roberts et al., 1995; Tauxe et al., 1996*] (Figure 4, e.g., sample cc1540–6580). Moreover, the measured  $M_r/M_s$  ratios are higher than in magnetite-bearing limestones from the literature [*Channell and McCabe, 1994*], approaching the reference values for a high coercivity contrast mixture (e.g., the pseudo-single domain magnetite-single domain hematite mixture of *Roberts et al. [1995]*) (Figure 5).

[15] Thermal (and AF) demagnetization data give insights also on changes in the relative proportions

of the 1.0 T and 0.1 T coercivity fractions with stratigraphic depth. In detail, the 1.0 T component shows higher values relative to the 0.1 T component in the middle part of RMZ 2 (i.e., approximately in the CMU), as well as in RMZ 4 from  $\sim 47$  m up to the section top. This datum is interpreted to indicate an increase of the hematite content of the samples (relative to pure maghemite) in correspondence of these intervals, as further illustrated in section 4.3.

[16] Finally, the pink-reddish to red sediments of RMZ 2–4 are characterized by the occasional occurrence of gray-greenish levels and spots (of diagenetic origin, see below). These levels and spots are dominated by a low (0.1 T) coercivity phase with maximum unblocking temperatures of  $\sim 575^\circ\text{C}$  and AF peak fields of 100 mT, interpreted

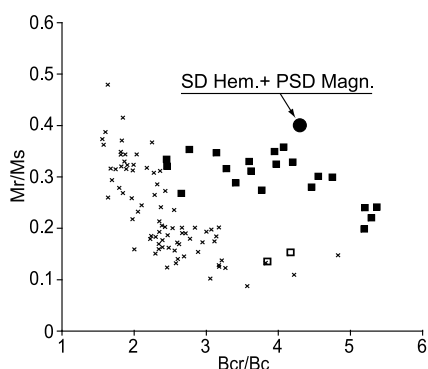


**Figure 5.** Plot of  $M_r/M_s$  versus  $B_{cr}/B_c$  ( $M_r$  = remanent magnetization;  $M_s$  = saturation magnetization;  $B_{cr}$  = coercivity of remanence;  $B_c$  = magnetic coercivity) of samples from the Cicogna section. Open squares refer to gray-greenish samples collected in the first ~15 m of the rock magnetic zone 1; black squares refer to pink-reddish to red samples collected from ~15 m upsection. The Cicogna sample distribution is compared to a reference distribution of hysteresis parameters (black crosses) obtained for magnetite-bearing (i.e., low coercivity) limestones from the literature [Channell and McCabe, 1994]. The black circle indicates the reference value for a PSD magnetite-SD hematite mixture of Roberts *et al.* [1995]. See text for details.

as magnetite. Subsidiary amounts of hematite with high coercivities (1.0 and 2.5 T) and maximum unblocking temperatures of up to 670°C have also been found in these samples (Figure 3c). The overall IRM intensity of the gray-greenish spots is approximately one order of magnitude lower than that of the surrounding red sediments, which are dominated by a hematite-maghemite mixture (Figure 3d).

### 4.3. IRM Spectra

[17] We summarize and further expand the discussion on the stratigraphic variability of the  $IRM_{0.1\text{ T}}$  and  $IRM_{1.0\text{ T}}$  values across the section originally provided by Dallanave *et al.* [2009]. Both parameters follow tightly the pattern of the low-field magnetic susceptibility (Figures 2a and 2b). In detail, low values characterize the basal ~20 m of RMZ 1, followed by higher values upsection, where the pink-reddish marls enriched in ferromagnetic (*s.l.*) minerals replace the marly limestone-marl couplets (Figure 2a). Both parameters show peak values at the RMZ 2 base (i.e., CMU onset), and a decreasing trend over the ensuing part of the CMU, interrupted by two marked negative shifts associated with the gray-greenish levels at ~29 m and ~30.8 m. Above, both parameters show a marked and persistent increasing trend starting at ~36 m

(RMZ 3 base) and peaking at ~42 m, to gradually decrease reaching relatively low and stable values from ~57 m within RMZ 4 upward. Discrete swings to higher values related to more marly layers punctuate this overall trend (e.g., at ~55 m, ~57 m, and ~73 m; Figure 2a).

[18] The  $IRM_{1.0/0.1\text{ T}}$  ratio shows generally low values within RMZ 1, whereas in RMZ 2, it shows a gradual increasing trend peaking at ~30.2 m, to remain relatively high and stable over the ensuing part of the CMU. Above the CMU, the  $IRM_{1.0/0.1\text{ T}}$  ratio gradually decreases, reaching pre-CMU values toward the top of RMZ 2 (Figures 2a and 2b). Above, it displays relatively low values across RMZ 3, to start increasing again from ~47 m up to ~74 m (RMZ 4) at the onset of deposition of the siliciclastic sediments of the Belluno Flysch (the formal base of which is placed at 80.6 m).

[19] Based also on the thermal and AF demagnetization data described above, we interpret the  $IRM_{1.0/0.1\text{ T}}$  ratio as a proxy of the hematite fraction concentration relative to pure maghemite (or magnetite in the first ~15 m of the section), whereby the lower the values, the lower the relative contribution of hematite to the IRM and *vice versa*. We can reasonably exclude a control on the  $IRM_{1.0/0.1\text{ T}}$  ratio exerted by goethite, which was not found in our thermal demagnetization experiments insofar as none of them showed the diagnostic loss of magnetization at 120°C along the high (2.5 T) coercivity axis [Özdemir and Dunlop, 1996]. From ~74 m on, the presence of sandy turbidites complicates the magnetic signal, and the  $IRM_{1.0/0.1\text{ T}}$  ratio can no longer be taken as representative of the relative hematite content of the sediments.

### 5. Detrital Versus Chemical Origin of the Magnetic Minerals

[20] The analyses reveal that the magnetic mineralogy of the gray-greenish basal ~15 m of RMZ 1 is dominated by magnetite, which coexists with subsidiary hematite. This magnetite is regarded as syndepositional in origin as it carries a primary paleomagnetic signal bearing polarity reversals [Dallanave *et al.*, 2009] retrieved in sediments with no obvious evidence of diagenetic reduction, which typically takes the form of lateral color changes within the sediment. The pink-reddish to red sediments from ~15 m upward are essentially dominated by mixtures of hematite grains (containing residual maghemitic phases) and pure maghemite grains, which are as well syndepositional in origin as

they carry a primary paleomagnetic signal [Dallanave *et al.*, 2009]. In particular, increased relative amounts of hematite are observed across RMZ 2 (i.e., between 28.7–36 m) and in RMZ 4 from ~47 m upsection.

[21] A detrital origin of these magnetic phases is supported by a strongly developed shallow bias of the characteristic paleomagnetic inclinations. The overall mean inclination at Cicogna was found to be ~25° shallower than the inclination expected at the site from the African apparent polar wander path (APWP) of Besse and Courtillot [2002], and was successfully corrected by Dallanave *et al.* [2009] using the elongation/inclination (E/I) method of Tauxe and Kent [2004] [see also Tauxe *et al.*, 2008]. A flattening factor of 0.4 was used for shallow bias correction, which is typical of sediments bearing detrital hematite [e.g., Tauxe and Kent, 1984].

[22] A (mainly) detrital origin of hematite differs from what previously observed in apparently similar Scaglia Rossa facies from classic sections of the Umbria Apennines near Gubbio. Here, Channell *et al.* [1982] documented the presence of antipodal magnetization components in samples from levels shortly below polarity reversal boundaries; a lower temperature component carried by magnetite of detrital (or biogenic) origin, which records the primary magnetization, is followed at higher temperatures by an antipodal component carried by hematite of diagenetic (post-polarity reversal) origin. Channell *et al.* [1982] interpreted these results as due to the protracted chemical nucleation during diagenesis of authigenic hematite phases derived from goethitic precursors within sediments originally containing primary detrital (or biogenic) magnetite. The orthogonal projection diagrams of the Cicogna red sediments do not show antipodal components across polarity reversal boundaries, and furthermore, there is no evidence in the Cicogna sediments of goethitic precursors. More importantly, the early Paleocene mean inclination of the Gubbio sediments ( $I = 42^\circ$  [Roggenthen and Napoleone, 1977]) is only ~6° shallower than the inclination expected at the site from the African APWP of Besse and Courtillot [2002] ( $I = 48^\circ$ ), strengthening the case for an authigenic origin of the hematite therein contained, whereby diagenetic hematite is typically less affected by inclination shallowing than detrital hematite. From the above we conclude that not all Scaglia Rossa facies are alike from a magnetic viewpoint whereby the Cicogna section seem to contain detrital hematite whereas the Gubbio section diagenetic hematite.

[23] Diagenesis does occur at Cicogna but is limited to the occasional gray-greenish levels and spots scattered within the red sediments of RMZ 2–4 described in section 4.2. The dominant magnetite phase present in these levels and spots may have derived from the post-depositional transformation of primary hematite and/or maghemite under reducing conditions [e.g., Özdemir and Dunlop, 1988; Torrent *et al.*, 2010]. Under such conditions, the newly formed magnetite can also undergo partial dissolution [Fischer *et al.*, 2007], as revealed by the anomalously low IRM intensity values that characterize these levels and spots compared to the surrounding sediments.

## 6. Climate Forcing on Sedimentation

[24] We infer that global climate change played a fundamental role in the formation, transport, and subsequent sedimentation of the observed magnetic iron oxides in the Cicogna section. The relative increase in detrital hematite revealed by the IRM<sub>1.0/0.1T</sub> curve in the CMU (i.e., PETM) and in the early Eocene can be related to enhanced chemical weathering rates during warm and humid climates [e.g., Dessert *et al.*, 2003; Schmitz and Pujalte, 2007] typical of these periods of time. Two of the most common iron oxides produced during continental weathering process are maghemite and hematite. Torrent *et al.* [2006] demonstrated the existence of a ferrihydrite → maghemite → hematite transformation pathway of weathering oxidation in continental aerobic environments. This model also predicts that the hematite/maghemite ratio (Hm/Mh) should increase with increasing degree of weathering. In this regard, Torrent *et al.* [2010, and references therein] studied sub-recent paleosols and found a relationship between the Hm/Mh ratio and mean annual temperature, whereby the higher the temperature, the higher the hematite formation relative to maghemite.

[25] To investigate our assumed relationship between rock magnetic variability and global climate, we migrated the IRM<sub>1.0/0.1T</sub> curve from Cicogna into the time domain for correlation with the late Paleocene–early Eocene benthic  $\delta^{18}\text{O}$  record of Zachos *et al.* [2001] using a slightly modified version of the age model of Dallanave *et al.* [2009]. We adopted a total of 7 magnetic polarity reversals as chronological control points from Chron C25n to Chron C23r, excluding the base of subchron C24n.3n, which is poorly resolved in the Cicogna section. As an additional tie-point, we used the base of

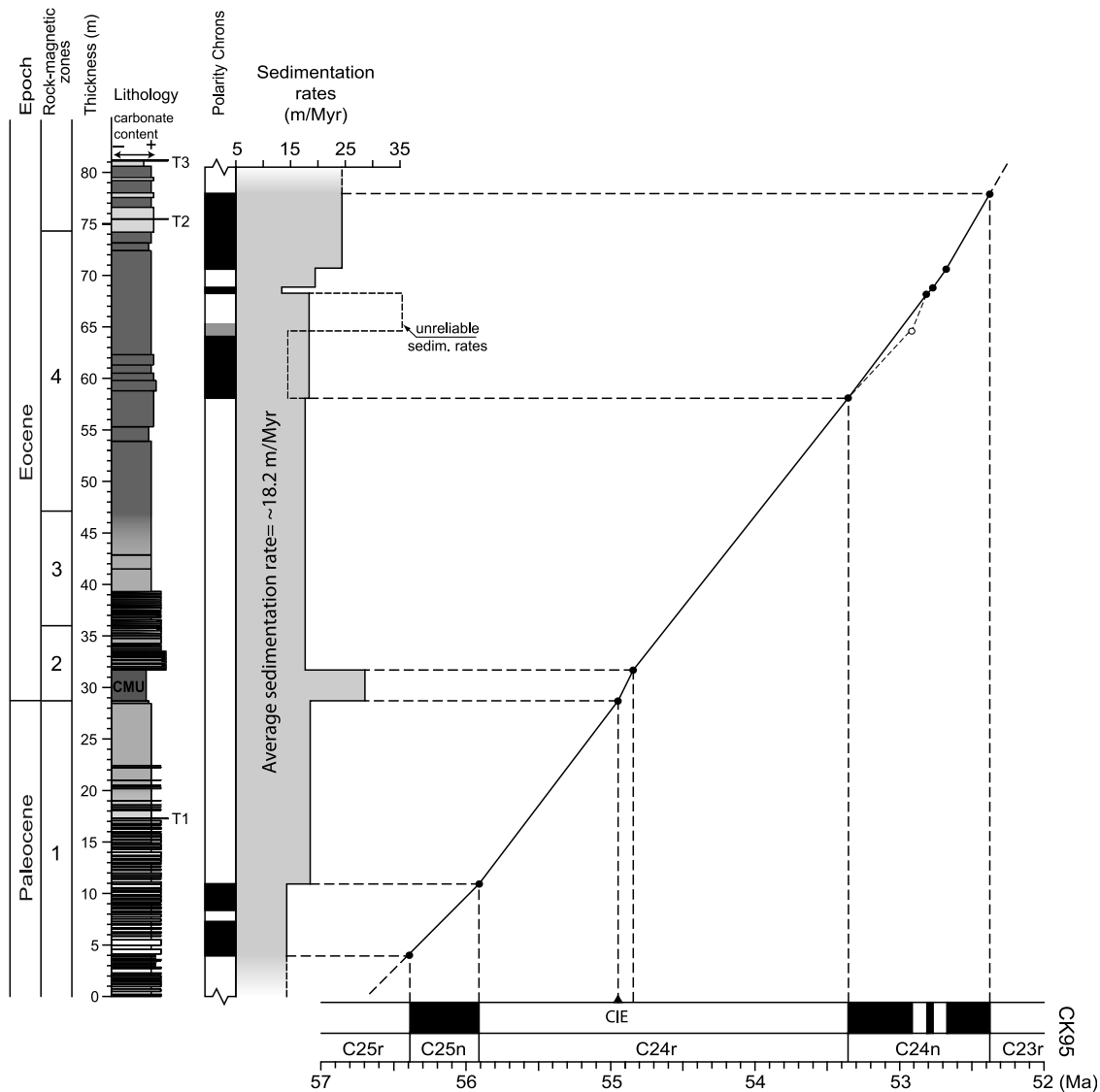


**Figure 6.** Age–depth model and derived sediment accumulation rates for the Cicogna section obtained by magnetostratigraphic correlation to the CK95 geomagnetic polarity time scale of *Cande and Kent* [1995]. See text for details.

the CMU (= Paleocene–Eocene boundary), which coincides with a  $\delta^{13}\text{C}$  negative excursion [Giusberti *et al.*, 2007]. We attributed an age of 54.95 Ma to the CMU base (Figure 6), which is the age of the base of the correlative global negative  $\delta^{13}\text{C}$  excursion adopted by Zachos *et al.* [2001]. Furthermore, Giusberti *et al.* [2007] used astrochronology to estimate a 105 kyr duration of the CMU in the nearby Forada section, which we adopt also for the similar CMU record at Cicogna. The new Cicogna age model implies relatively constant average sediment accumulation rates of  $\sim 18$  m/Myr, save for the 3 m-thick CMU, with rates of up to  $\sim 29$  m/Myr, and the uppermost

$\sim 10$  m of the section, where accumulation rates reach values of  $\sim 24.5$  m/Myr (Figure 6).

[26] We evaluated the robustness of the correlation between the  $\text{IRM}_{1.0/0.1\text{T}}$  and the  $\delta^{18}\text{O}$  time series using the coherence function, which is the generalization of the correlation coefficient to the frequency domain. We first calculated the additive inverse of the  $\delta^{18}\text{O}$  values, creating a new set of data equally spaced in time by 23.4 kyr (which is the mean temporal resolution of the  $\delta^{18}\text{O}$  data set in the late Paleocene–early Eocene). Next, we generated a new  $\text{IRM}_{1.0/0.1\text{T}}$  curve adopting the same (23.4 kyr) time spacing of the  $\delta^{18}\text{O}$  curve

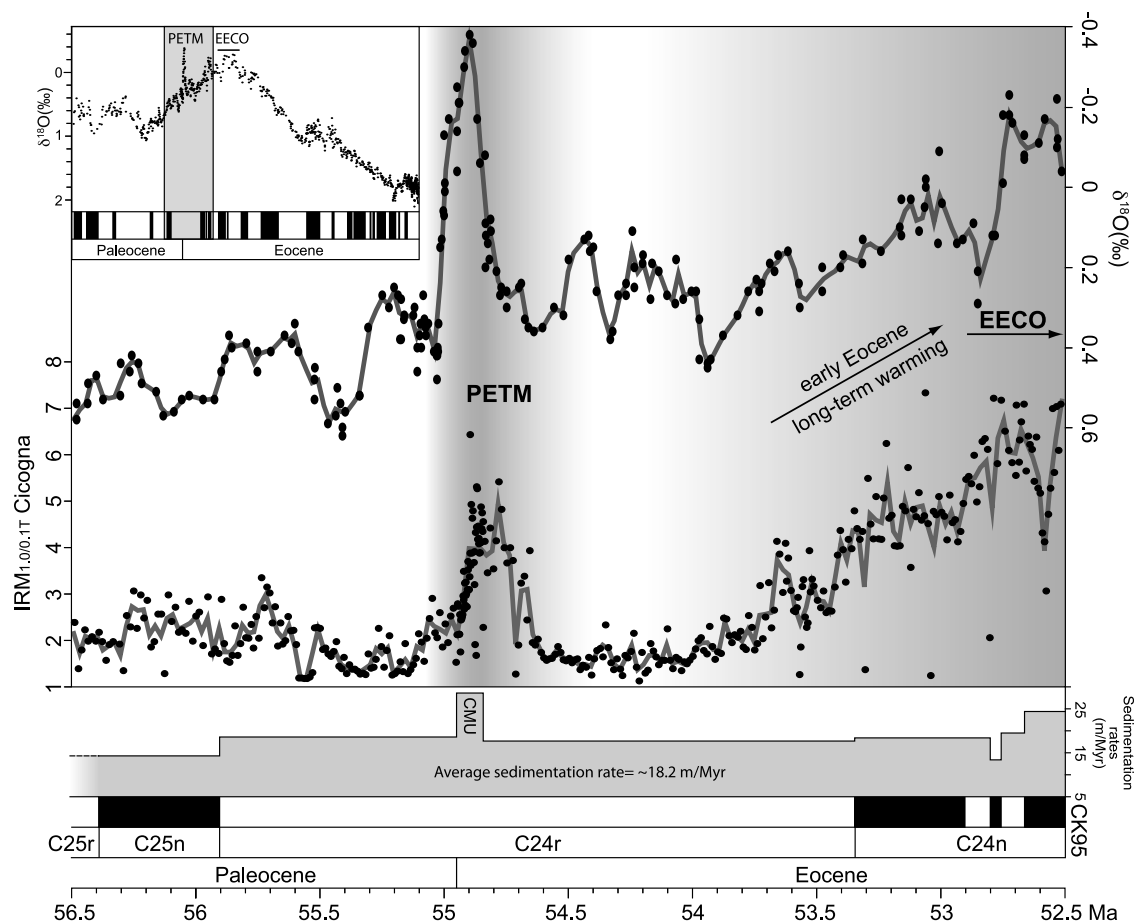


**Figure 7.** The Cicogna  $IRM_{1.0/0.1T}$  data set compared with the  $\delta^{18}O$  record of *Zachos et al.* [2001] across the late Paleocene–early Eocene. Both data sets are placed onto the same time scale (CK95 [Cande and Kent, 1995]); the dark-gray curves behind the black dots represent the data set used to calculate the coherence parameters. The Cicogna sediment accumulation rates are also shown on the CK95 time scale. The inset shows the  $\delta^{18}O$  curve up to the Eocene–Oligocene boundary with indication (gray band) of the time interval spanned by the Cicogna section. See text for details.

(Figure 7). The range of frequencies for which the  $IRM_{1.0/0.1T}$  data are coherent with the paleotemperatures proxy is readily visible from the plot of the squared coherence between the two data set [Tauxe and Wu, 1990] (Figure 8). We assigned a squared coherence minimum value of 0.038 as 95% level of confidence, calculated using the relation given by Chave and Filloux [1985]. As shown in Figure 8, the two records show coherence over the 0–6.3  $Myr^{-1}$  range of frequencies, as well as between 10.6–11.3  $Myr^{-1}$ ; the highest values of squared coherence is reached at the 0 frequency, which implies a linear correlation between the two data sets along the  $\sim 4$  Myr duration of the time series. The second peak of the squared coherence at the 4.75  $Myr^{-1}$  frequency corresponds to the correlation along a wavelength of  $\sim 210$  kyr, which is approximately the

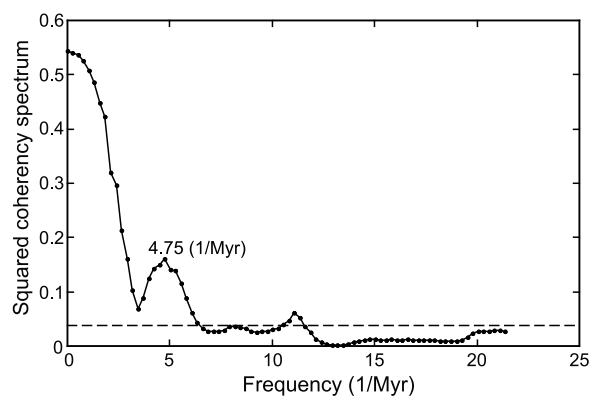


**Figure 8.** Squared coherence between the  $IRM_{1.0/0.1T}$  record from the Cicogna section and the  $\delta^{18}O$  record of *Zachos et al.* [2001]. The dashed line represents the 95% confidence level. See text for details.

duration of the oxygen isotopes excursion that occurred during the PETM.

[27] According to this analysis, higher  $IRM_{1.0/0.1T}$  ratios typical of red sediments enriched in primary hematite (relative to magnetite or pure maghemite) statistically correlate to the warm climate conditions of the PETM as well as the warming trend leading to the EECO, whereas lower ratios typical of sediments with lower amounts of hematite correlate with relatively cooler climate conditions, e.g., in the late Paleocene (Figure 7). This scenario of climate forcing on sedimentation is further strengthened by the higher sediment accumulation rates registered in the Cicogna section across the CMU (i.e., the PETM) and generally in the upper part of the section of early Eocene age (Figures 6 and 7), which are compatible with enhanced continental runoff rates typical of these warm and humid climate conditions.

## 7. Conclusions

[28] We believe that the tight temporal coupling between rock magnetic properties and global climate observed at Cicogna agrees with the climate stabilization mechanism first described by Walker *et al.* [1981]. According to this model, carbon dioxide, which is released by volcanoes and metamorphism to the ocean-atmosphere system, is returned to the solid earth by the weathering of silicates followed by the deposition of carbonates. The intensity of the weathering depends on the surface temperatures, which in turn depend on carbon dioxide partial pressure ( $pCO_2$ ) through the greenhouse effect [Walker *et al.*, 1981; Velbel, 1993; Kump *et al.*, 2000]. The rate of silicate weathering therefore provides a negative feedback mechanism to buffer  $pCO_2$  variations and consequently Earth's climate change, and the signature of this mechanism is apparently registered in the Belluno Basin by the deposition of detrital magnetic phases with oxidation states determined by the intensity of the weathering processes on land.

## Acknowledgments

[29] We thank Dennis Kent and reviewers José Torrent and Massimo Mattei for valuable comments that greatly improved this manuscript. E. Dallanave and D. Rio were supported by MIUR-PRIN grant 2007W9B2WE\_004. Acknowledgment is made to the Donors of the American Chemical Society Petroleum Research Fund for partial support of this research in the SIO laboratory.

## References

- Agnini, C., G. Muttoni, D. V. Kent, and D. Rio (2006), Eocene biostratigraphy and magnetic stratigraphy from Possagno, Italy: The calcareous nannofossils response to climate variability, *Earth Planet. Sci. Lett.*, *241*, 815–830, doi:10.1016/j.epsl.2005.11.005.
- Arenillas, I., E. Molina, and B. Schmitz (1999), Planktic foraminiferal and  $\delta^{13}C$  isotopic changes across the Paleocene/Eocene boundary at Possagno (Italy), *Int. J. Earth Sci.*, *88*, 352–364, doi:10.1007/s005310050270.
- Berggren, W. A., D. V. Kent, C. C. Swisher III, and M.-P. Aubry (1995), A revised Cenozoic geochronology and chronostratigraphy, in *Geochronology, Time Scales and Global Stratigraphy Correlation*, edited by W. A. Berggren *et al.*, *Spec. Publ. SEPM Soc. Sediment. Geol.*, *54*, 129–212.
- Besse, J., and V. Courtillot (2002), Apparent and true polar wander and the geometry of the geomagnetic field over the last 200 Myr, *J. Geophys. Res.*, *107*(B11), 2300, doi:10.1029/2000JB000050. (Correction, *J. Geophys. Res.*, *108*(B10), 2469, doi:10.1029/2003JB002684, 2003.)
- Bolle, M.-P., and T. Adate (2001), Paleocene–early Eocene climatic evolution in the Tethyan realm: Clay mineral evidence, *Clay Miner.*, *36*, 249–261, doi:10.1180/000985501750177979.
- Bowen, G. J., D. J. Beerling, P. L. Koch, J. C. Zachos, and T. Quattlebaum (2004), A humid climate state during the Paleocene/Eocene thermal maximum, *Nature*, *432*, 495–499, doi:10.1038/nature03115.
- Bralower, T. J., J. C. Zachos, E. Thomas, M. Parrow, K. Paull, D. C. Kelly, I. Premoli Silva, W. V. Sliter, and K. C. Lohmann (1995), Late Paleocene to Eocene paleoceanography of the equatorial Pacific Ocean: Stable isotopes recorded at Ocean Drilling Program Site 865, Allison Guyot, *Paleoceanography*, *10*(4), 841–865, doi:10.1029/95PA01143.
- Cande, S. C., and D. V. Kent (1995), Revised calibration of the geomagnetic polarity time scale for the Late Cretaceous and Cenozoic, *J. Geophys. Res.*, *100*(B4), 6093–6096, doi:10.1029/94JB03098.
- Castellarin, A., and L. Cantelli (2000), Neo-Alpine evolution of the Southern Eastern Alps, *J. Geodyn.*, *30*, 251–274, doi:10.1016/S0264-3707(99)00036-8.
- Channell, J. E. T., and C. McCabe (1994), Comparison of magnetic hysteresis parameters of unremagnetized and remagnetized limestones, *J. Geophys. Res.*, *99*(B3), 4613–4623, doi:10.1029/93JB02578.
- Channell, J. E. T., R. Freeman, F. Heller, and W. Lowrie (1982), Timing of diagenetic haematite growth in red pelagic limestones from Gubbio (Italy), *Earth Planet. Sci. Lett.*, *58*, 189–201, doi:10.1016/0012-821X(82)90193-5.
- Chave, A. D., and J. H. Filloux (1985), Observation and interpretation of the seafloor vertical electric field in the eastern North Pacific, *Geophys. Res. Lett.*, *12*, 793–796, doi:10.1029/GL012i012p00793.
- Costa, V., C. Doglioni, P. Grandesso, D. Masetti, G. B. Pellegrini, and E. Tracanella (1996), Belluno, with explanatory text, *Carta Geol. d'Italia, Sheet 063*, scale 1:50,000, Ital. Geol. Surv., Rome.
- Cramer, B. S., and D. V. Kent (2005), Bolide summer: The Paleocene/Eocene thermal maximum as a response to an extraterrestrial trigger, *Palaeogeogr. Palaeoclimatol. Palaeoecol.*, *224*, 144–166, doi:10.1016/j.palaeo.2005.03.040.
- Cramer, B. S., J. D. Wright, D. V. Kent, and M.-P. Aubry (2003), Orbital climate forcing of  $\delta^{13}C$  excursions in the late Paleocene–early Eocene (chrons C24n–C25n), *Paleoceanography*, *18*(4), 1097, doi:10.1029/2003PA000909.



- Dallanave, E., C. Agnini, G. Muttoni, and D. Rio (2009), Magneto-biostratigraphy of the Cicogna section (Italy): Implication for the late Paleocene–early Eocene time scale, *Earth Planet. Sci. Lett.*, *285*, 39–51, doi:10.1016/j.epsl.2009.05.033.
- Dessert, C., B. Dupre, J. Gaillardet, L. M. Francois, and C. J. Allegre (2003), Basalt weathering laws and the impact of basalt weathering on the global carbon cycle, *Chem. Geol.*, *202*, 257–273, doi:10.1016/j.chemgeo.2002.10.001.
- Dickens, G. R., J. R. O’Neil, D. K. Rea, and R. M. Owen (1995), Dissociation of oceanic methane hydrate as a cause of the carbon isotope excursion at the end of the Paleocene, *Paleoceanography*, *10*(6), 965–971, doi:10.1029/95PA02087.
- Di Napoli Alliata, E., F. Proto Decima, and G. B. Pellegrini (1970), Studio geologico, stratigrafico e micropaleontologico dei dintorni di Belluno, *Mem. Soc. Geol. Ital.*, *9*, 1–28.
- Dingle, R. V., S. A. Marenssi, and M. Lavelle (1998), High latitude Eocene climate deterioration: Evidence from the northern Antarctic Peninsula, *J. South Am. Earth Sci.*, *11*(6), 571–579, doi:10.1016/S0895-9811(98)00035-2.
- Fischer, H., J. Lustre, and A. U. Gehring (2007), EPR evidence for maghemitization of magnetite in a tropical soil, *Geophys. J. Int.*, *169*, 909–916, doi:10.1111/j.1365-246X.2007.03311.x.
- Giusberti, L., D. Rio, C. Agnini, J. Backman, E. Fornaciari, F. Tateo, and M. Oddone (2007), Mode and tempo of the Paleocene–Eocene thermal maximum in an expanded section from the Venetian pre-Alps, *Geol. Soc. Am. Bull.*, *119*, 391–412, doi:10.1130/B25994.1.
- Kelly, D. C., T. J. Bralower, J. C. Zachos, I. Premoli Silva, and E. Thomas (1996), Rapid diversification of planktonic foraminifera in the tropical Pacific (ODP Site 865) during the late Paleocene thermal maximum, *Geology*, *24*, 423–426, doi:10.1130/0091-7613(1996)024<0423:RDOPFI>2.3.CO;2.
- Kennett, J. P., and L. D. Stott (1991), Abrupt deep-sea warming, paleoceanographic changes and benthic extinctions at the end of the Paleocene, *Nature*, *353*, 225–229, doi:10.1038/353225a0.
- Kent, D. V., and G. Muttoni (2008), Equatorial convergence of India and early Cenozoic climate trends, *Proc. Natl. Acad. Sci. U. S. A.*, *105*(42), 16,065–16,070, doi:10.1073/pnas.0805382105.
- Kent, D. V., B. S. Cramer, L. Lanci, D. Wang, J. D. Wright, and R. Van der Voo (2003), A case for a comet impact trigger for the Paleocene/Eocene thermal maximum and carbon isotope excursion, *Earth Planet. Sci. Lett.*, *211*, 13–26, doi:10.1016/S0012-821X(03)00188-2.
- Koch, P. L., J. C. Zachos, and P. D. Gingerich (1992), Correlation between isotope records in marine and continental carbon reservoirs near the Palaeocene/Eocene boundary, *Nature*, *358*, 319–322, doi:10.1038/358319a0.
- Kodama, K. P. (1982), Magnetic effects of maghemitization of Plio–Pleistocene marine sediments, northern California, *J. Geophys. Res.*, *87*(B8), 7113–7125, doi:10.1029/JB087iB08p07113.
- Kump, L. R., S. L. Brantley, and M. A. Arthur (2000), Chemical weathering, Atmospheric CO<sub>2</sub>, and climate, *Annu. Rev. Earth Planet. Sci.*, *28*, 611–667, doi:10.1146/annurev.earth.28.1.611.
- Lowenstein, T. K., and R. V. Demicco (2006), Elevated Eocene atmospheric CO<sub>2</sub> and its subsequent decline, *Science*, *313*, 1928–1929, doi:10.1126/science.1129555.
- Lowrie, W. (1990), Identification of ferromagnetic minerals in a rock by coercivity and unblocking temperature properties, *Geophys. Res. Lett.*, *17*, 159–162, doi:10.1029/GL017i002p00159.
- McKenna, M. C. (1980), Eocene paleolatitude, climate, and mammals of Ellesmere Island, *Palaeogeogr. Palaeoclimatol. Palaeoecol.*, *30*, 349–362, doi:10.1016/0031-0182(80)90065-6.
- Miller, K. G., J. D. Wright, and R. G. Fairbanks (1991), Unlocking the ice house: Oligocene–Miocene oxygen isotopes, eustasy, and margin erosion, *J. Geophys. Res.*, *96*, 6829–6848, doi:10.1029/90JB02015.
- Miller, K. G., J. D. Wright, and J. V. Browning (2005), Visions of ice sheets in a greenhouse world, *Mar. Geol.*, *217*, 215–231, doi:10.1016/j.margeo.2005.02.007.
- Moran, K., et al. (2006), The Cenozoic palaeoenvironment of the Arctic Ocean, *Nature*, *441*, 601–605, doi:10.1038/nature04800.
- Muttoni, G. (1995), “Wasp-waisted” hysteresis loops from a pyrrhotite and magnetite-bearing remagnetized Triassic limestone, *Geophys. Res. Lett.*, *22*(23), 3167–3170, doi:10.1029/95GL03073.
- Muttoni, G., and D. V. Kent (2007), Widespread formation of cherts during the early Eocene climate optimum, *Palaeogeogr. Palaeoclimatol. Palaeoecol.*, *253*, 348–362, doi:10.1016/j.palaeo.2007.06.008.
- Özdemir, Ö., and D. J. Dunlop (1988), Crystallization remanent magnetization during the transformation of maghemite to hematite, *J. Geophys. Res.*, *93*(B6), 6530–6544, doi:10.1029/JB093iB06p06530.
- Pagani, M., J. C. Zachos, K. H. Freeman, B. Tipler, and S. Bohaty (2005), Marked decline in atmospheric carbon dioxide concentrations during the Paleogene, *Science*, *309*, 600–603, doi:10.1126/science.1110063.
- Pagani, M., K. Caldeira, D. Archer, and J. C. Zachos (2006), An ancient carbon mystery, *Science*, *314*, 1556–1557, doi:10.1126/science.1136110.
- Pearson, P. N., P. Ditchfield, J. Singano, K. G. Harcourt-Brown, C. J. Nicholas, R. K. Olsson, N. Shackleton, and M. A. Hall (2001), Warm tropical sea surface temperatures in the Late Cretaceous and Eocene epochs, *Nature*, *413*, 481–487, doi:10.1038/35097000.
- Robert, C., and J. P. Kennett (1994), Antarctic subtropical humid episode at the Paleocene–Eocene boundary: Clay-mineral evidence, *Geology*, *22*, 211–214, doi:10.1130/0091-7613(1994)022<0211:ASHEAT>2.3.CO;2.
- Roberts, A. P., Y. Cui, and K. L. Verosub (1995), Wasp-waisted hysteresis loops: Mineral characteristic and discrimination of components in mixed magnetic systems, *J. Geophys. Res.*, *100*(B9), 17,909–17,924, doi:10.1029/95JB00672.
- Roggenthen, W. M., and G. Napoleone (1977), The Gubbio section: Upper Cretaceous–Paleocene magnetic stratigraphy, *Geol. Soc. Am. Bull.*, *88*, 378–382, doi:10.1130/0016-7606(1977)88<378:UCMSAG>2.0.CO;2.
- Röhl, U., T. Westerhold, T. J. Bralower, and J. C. Zachos (2007), On the duration of the Paleocene–Eocene thermal maximum (PETM), *Geochem. Geophys. Geosyst.*, *8*, Q12002, doi:10.1029/2007GC001784.
- Schmitz, B., and V. Pujalte (2007), Abrupt increase in seasonal extreme precipitation at the Paleocene–Eocene boundary, *Geology*, *35*, 215–218, doi:10.1130/G23261A.1.
- Sloan, L. C., and D. K. Rea (1996), Atmospheric carbon dioxide and early Eocene climate: A general circulation modeling sensitivity study, *Palaeogeogr. Palaeoclimatol. Palaeoecol.*, *119*, 275–292, doi:10.1016/0031-0182(95)00012-7.
- Svensen, H., S. Planke, A. Malthe-Sørensen, B. Jamteveit, R. Myklebust, T. Rasmussen Eidem, and S. S. Rey (2004),

- Release of methane from a volcanic basin as a mechanism for initial Eocene global warming, *Nature*, *429*, 542–545, doi:10.1038/nature02566.
- Tauxe, L. (2010), *Essentials of Paleomagnetism*, Univ. of Calif. Press, Berkeley.
- Tauxe, L., and D. V. Kent (1984), Properties of detrital remanence carried by hematite from study of modern river deposits and laboratory redeposition experiments, *Geophys. J. R. Astron. Soc.*, *76*, 543–561.
- Tauxe, L., and D. V. Kent (2004), A simplified statistical model for the geomagnetic field and the detection of shallow bias in paleomagnetic inclinations: Was the ancient magnetic field dipolar?, in *Timescales of the Paleomagnetic Field*, *Geophys. Monogr. Ser.*, vol. 145, edited by J. E. T. Channell et al., pp. 101–115, AGU, Washington, D. C.
- Tauxe, L., and G. Wu (1990), Normalized remanence in sediments of the western equatorial Pacific: Relative paleointensity of the geomagnetic field?, *J. Geophys. Res.*, *95*(B8), 12,337–12,350, doi:10.1029/JB095iB08p12337.
- Tauxe, L., T. A. T. Mullender, and T. Pick (1996), Potbellies, wasp-waists, and superparamagnetism in magnetic hysteresis, *J. Geophys. Res.*, *101*(B1), 571–583, doi:10.1029/95JB03041.
- Tauxe, L., K. P. Kodama, and D. V. Kent (2008), Testing corrections for paleomagnetic inclination error in sedimentary rocks: A comparative approach, *Phys. Earth Planet. Inter.*, *169*, 152–165, doi:10.1016/j.pepi.2008.05.006.
- Thomas, D. J., and T. J. Bralower (1999), New evidence for subtropical warming during the late Paleocene thermal maximum: Stable isotopes from Deep Sea Drilling Project Site 527, Walvis Ridge, *Paleoceanography*, *14*(5), 561–570, doi:10.1029/1999PA900031.
- Thomas, E., and N. J. Shackleton (1996), The Paleocene–Eocene benthic foraminiferal extinction and stable isotope anomalies, in *Correlation in the Early Paleogene in Northwest Europe*, edited by R. W. O’B. Knox et al., *Geol. Soc. Spec. Publ.*, *101*, 401–441.
- Torrent, J., V. Barrón, and Q. Liu (2006), Magnetic enhancement is linked to and precedes hematite formation in aerobic soil, *Geophys. Res. Lett.*, *33*, L02401, doi:10.1029/2005GL024818.
- Torrent, J., Q. S. Liu, and V. Barrón (2010), Magnetic susceptibility changes in relation to pedogenesis in a Xeralf chronosequence in northwestern Spain, *Eur. J. Soil Sci.*, *61*, 161–173, doi:10.1111/j.1365-2389.2009.01216.x.
- Velbel, M. A. (1993), Temperature dependence of silicate weathering in nature: How strong a negative feedback on long-term accumulation of atmospheric CO<sub>2</sub> and global greenhouse warming?, *Geology*, *21*, 1059–1062, doi:10.1130/0091-7613(1993)021<1059:TDOSWI>2.3.CO;2.
- Walker, J. C. G., P. B. Hays, and J. F. Kasting (1981), A negative feedback mechanism for the long-term stabilization of the Earth’s surfaces temperature, *J. Geophys. Res.*, *86*, 9776–9782, doi:10.1029/JC086iC10p09776.
- Wang, X., Z. Yang, R. Løvlie, and L. Min (2004), High-resolution magnetic stratigraphy of fluvio-lacustrine succession in the Nihewan Basin, China, *Quat. Sci. Rev.*, *23*, 1187–1198, doi:10.1016/j.quascirev.2003.11.007.
- Winterer, E. L., and A. Bosellini (1981), Subsidence and sedimentation on Jurassic passive continental margin, Southern Alps, Italy, *Am. Assoc. Pet. Geol. Bull.*, *65*, 394–421.
- Yapp, C. J. (2004), Fe(CO<sub>3</sub>)OH in goethite from a mid-latitude North American Oxisol: Estimate of atmospheric CO<sub>2</sub> concentration in the early Eocene “climatic optimum,” *Geochim. Cosmochim. Acta*, *68*(5), 935–947, doi:10.1016/j.gca.2003.09.002.
- Zachos, J. C., M. Pagani, L. Sloan, E. Thomas, and K. Billups (2001), Trends, rhythms and aberrations in global climate 65 Ma to present, *Science*, *292*, 686–693, doi:10.1126/science.1059412.
- Zachos, J. C., M. W. Wara, S. Bohaty, M. L. Delaney, M. R. Petrizzo, A. Brill, T. J. Bralower, and I. Premoli Silva (2003), A transient rise in tropical sea surface temperature during the Paleocene–Eocene thermal maximum, *Science*, *302*, 1551–1554, doi:10.1126/science.1090110.
- Zachos, J. C., et al. (2005), Rapid acidification of the ocean during the Paleocene–Eocene thermal maximum, *Science*, *308*, 1611–1615, doi:10.1126/science.1109004.